Article

Not peer-reviewed version

A Significant Decrease in Thermal Conductivity in Eu- and Cd-Doped ZnO Films due to the Inhomogeneity of Impurities

Misha Khalid , Hadiqa Naaz , Ameneh Mkaeeli , Ibtasam Bin Abdul Ghani , Misbah Aslam , E. Przezdziecka , H. Mubeen , R. Jakieła , A. Wierzbicka , B. Witkowski , Carlos J. Tavares , Andreas D. Wieck , Michal Pawlak *

Posted Date: 17 March 2026

doi: 10.20944/preprints202603.1194.v1

Keywords: films; ZnO

 doi:10.20944/preprints202603.1194.v1

Article

A Significant Decrease in Thermal Conductivity in Eu- and Cd-Doped ZnO Films Due to the Inhomogeneity of Impurities

Misha Khalid [1], Hadiqa Naaz [1], Ameneh Mikaeeli [1,2], Ibtasam Bin Abdul Ghani [3], Misbah Aslam [4], E. Przeździecka [5], H. Mubeen [5], R. Jakieła [5], A. Wierzbick [5], B. Witkowski [5], Carlos J. Tavares [6], Andreas D. Wieck [7] and Michał Pawlak [1,*]

[1] Institute of Physics, Faculty of Physics, Astronomy, and Informatics, Nicolaus Copernicus University, Grudziadzka 5, 87-100, Torun, Poland

[2] Chair of Applied Solid-State Physics, Experimental Physics VI, Ruhr-University Bochum, Universitaetsstrasse 150, D-44780, Bochum, Germany

[3] Key Laboratory of Advance Technologies of Materials, Ministry of Education, College of Medicine, School of Materials Science and Engineering, Southwest Jiaotong University, Chengdu 610031, PR China

[4] Department of Physics, Quaid-i-Azam University Islamabad, National Center for Physics Islamabad-44000, Pakistan.

[5] Institute of Physics, Polish Academy of Science, Al. Lotników 32/46, 02-668, Warsaw, Poland

[6] Centre of Physics of Minho and Porto Universities (CF-UM-UP), University of Minho, 4804-533 Guimaraes, Portugal

* Correspondence: Author: Prof. Michal Pawlak (mpawlak@umk.pl)

Abstract

We demonstrate that dopant inhomogeneity strongly suppresses thermal conductivity in Cd/Eu co-doped, non-polar *a*-oriented ZnO films grown on *r*-plane sapphire (Al_2O_3) by plasma-assisted molecular beam epitaxy. Structural characterization by θ-2θ XRD confirms *a*-oriented ZnO without detectable secondary phases. Cross-sectional SEM shows continuous films with well-defined interfaces, and SIMS depth profiling verifies Cd/Eu incorporation through the film thickness and a sharp Zn/O drop at the substrate interface. Optical transmittance and Tauc analysis reveal composition-dependent shifts of the absorption edge and band gap. Cross-plane thermal transport was measured at room temperature using frequency-domain photothermal infrared radiometry (PTR) and analyzed by fitting the complex PTR amplitude and phase with a multilayer heat-diffusion model. The extracted thermal conductivity spans ~3.7 - 6.3 $W \cdot m^{-1} \cdot K^{-1}$. The lowest *k* values correlate with increased defect non-uniformity, consistent with enhanced phonon scattering and reduced effective cross-plane heat transport.

Keywords: films; ZnO

Introduction

Metal oxide semiconductors, including zinc oxide (ZnO), titanium dioxide (TiO_2) and selenium dioxide (SeO_2) have been extensively investigated [1]. Their wide band gaps, chemical stability, and tunable electrical and thermal properties make them important functional materials. Among these, zinc oxide (ZnO), a II–VI semiconductor has been extensively studied since the mid-20th century [2]. Its favorable bulk properties including high electron mobility, superior thermal and chemical stability, natural abundance and low toxicity, render it a strong candidate for optoelectronic, sensing and thermoelectric applications [3]. For thermoelectric applications, material performance is evaluated using the dimensionless figure of merit $ZT = \frac{S^2 \sigma T}{\kappa}$ where, S denotes the Seebeck

 doi:10.20944/preprints202603.1194.v1

coefficient, σ the electrical conductivity, T the absolute temperature, and κ the total thermal conductivity [4]. Consequently, achieving low thermal conductivity without compromising electrical transport is a central challenge in the optimization of ZnO-based thermoelectric materials.

In recent years, ZnO nanostructures and thin films have gained increasing attention for energy harvesting and thermal management applications [5]. ZnO crystallizes primarily in the hexagonal wurtzite structure, although cubic zinc blende phases have also been reported under specific growth conditions [6]. Various synthesis techniques including pulsed laser deposition, magnetron sputtering, molecular beam epitaxy (MBE), sol gel processing, hydrothermal growth and solid-state reactions enable precise control over morphology, crystallinity and defect chemistry [7]. Among these methods plasma-assisted molecular beam epitaxy (PA-MBE) offers exceptional control over growth parameters and dopant incorporation, making it particularly suitable for investigating subtle compositional effects on structural and physical properties [8].

Doping is an effective strategy for tailoring ZnOs thermal and electronic behavior. Incorporation of transition metals and rare-earth elements modifies lattice dynamics, carrier concentration and phonon transport mechanisms [9]. Cadmium (Cd), a group II transition metal with a larger ionic radius (0.97 Å) than Zn^{2+} (0.74 Å), can substitute isovalently into the ZnO lattice, leading to lattice expansion and changes in phonon dispersion [10]. At low concentrations, Cd incorporation may alter phonon mean free paths, while higher levels introduce disorder-driven phonon scattering [11]. Rare-earth dopants, such as europium (Eu), typically incorporate as Eu^{3+} ions and introduce localized 4f electronic states. These ions create point defects and lattice distortions that enhance phonon-impurity and Umklapp scattering at higher temperatures, effectively reducing the lattice contribution to thermal conductivity [12].

Previous studies have demonstrated that controlled doping of ZnO with transition metals and lanthanides can significantly influence its optical, structural and thermal properties [9]. In particular, rare-earth-doped ZnO systems have shown suppressed thermal conductivity alongside modified band gaps and characteristic luminescence related to dopant ions [13]. However, most reported studies focus on bulk ceramics or nanopowders, while fewer investigations address epitaxial, non-polar ZnO thin films grown by MBE, where anisotropic strain and defect distributions may play a crucial role [14].

Doping of ZnO thin layers is a promising strategy for thermoelectric applications because it enables the reduction of thermal conductivity while maintaining favorable electrical transport. In rare-earth-doped GeTe, the decrease in thermal conductivity originates from strong mass and strain-field fluctuations introduced by heavy rare-earth ions. For example, Eu doping in GeTe significantly suppresses lattice heat transport, with the thermal conductivity decreasing from ~4.0 $W \cdot m^{-1} \cdot K^{-1}$ to ~3.0 $W \cdot m^{-1} \cdot K^{-1}$ after Eu doping, mainly due to enhanced phonon scattering and lattice softening [15]. In Ce-doped ZnO, the reduction in thermal conductivity is attributed to impurity induced point defects, lattice distortion, and a decrease in Young's modulus, which collectively shorten the phonon mean free path and suppress lattice thermal conductivity [16]. Similarly, in Bi and Al-doped ZnO thin films, different scattering mechanisms dominate, Al substitution reduces thermal conductivity via alloy phonon scattering in the ZnO wurtzite lattice, lowering k from ~6.0 to ~3.3 $W \cdot m^{-1} \cdot K^{-1}$. In contrast, Bi doping reduces k primarily through grain boundary scattering, as Bi segregates at grain-boundary triple points, leading to a further reduction to ~2.9 $W \cdot m^{-1} \cdot K^{-1}$ in ZnO:Al,Bi films [17]. These studies demonstrate that dopant mass, defect chemistry, and microstructural evolution play critical roles in suppressing thermal conductivity in thermoelectric materials.

In this study, we investigate the structural, morphological and optical properties of non-polar *a*-oriented ZnO thin films co-doped in situ with trace amounts of Cd and Eu. The samples were synthesized on *r*-plane sapphire substrates utilizing PA-MBE. While previous research has predominantly addressed single-dopant systems to enhance thermoelectric performance, this work explores the simultaneous incorporation of a transition metal and a rare-earth ion. We demonstrate that even at dopant concentrations near the detection limit, the synergistic effect of Cd and Eu significantly modifies the lattice parameters and produces a substantial carrier concentration of

 doi:10.20944/preprints202603.1194.v1

approximately 5 × 10^{19} cm^{-3}. The resulting shifts in the optical band gap and the distinct europium-related luminescence emissions underscored the sensitivity of the ZnO electronic structure to dual-doping. Ultimately, these results established a foundation for utilizing trace co-doping architectures to optimize the figure of merit (ZT) in wide-bandgap semiconductors for thermoelectric [18] and optoelectronic applications.

Samples

In situ ZnO:Cd,Eu films were grown on commercially available *r*-plane sapphire substrates using plasma assisted molecular beam epitaxy (PA-MBE) in a Riber Compact 21 system. The *r*-plane sapphire (Al_2O_3) substrates were chemically cleaned in a H_2SO_4:H_2O_2 (1:1) mixture for 5 minutes before growth. For thermal purification the substrates were annealed at a temperature of 150 °C for 1 hour in the loading chamber and then the substrates were transferred to the growth chamber followed by vacuum annealing at 700 °C and then for 30 minutes in an oxygen (O_2) plasma. During the growth process, the radiofrequency (RF) power of the oxygen plasma was maintained at 240 W with an O_2 gas flow rate of 3 sccm. All ZnO:Cd,Eu samples were grown at 360 °C, as measured by a thermocouple. High purity Zn (6 N), Cd (6 N), and Eu (4 N) elements were used as sources from the Knudsen effusion cells. The Beam Equivalent Pressure (BEP), defined as a local pressure of a Zn and Cd and Eu directional gas beam on a substrate surface (namely fluxes), was *measured by a pressure gauge*. The details of the growth parameters in analysed samples are presented in Table 1.

Table 1. Growth parameters of the oxide samples; Zn, Cd and Eu fluxes.

Sample name	Zn Flux (×10^{-7} Torr)	Cd Flux (×10^{-8} Torr)	Eu Flux (×10^{-9} Torr)
z12AR	9.72	4.00	1.11
z121BR	9.72	6.00	0.05
z13R	9.17	3.25	0.97
z1124R	9.85	7.20	4.73

Methods

Thermal conductivity measurements were carried out using photothermal infrared radiometry (PTR) system schematically shown in Figure 1. A DPSS laser (CNI MGL-FN-532-1W, 532 nm, 800 mW) served as the excitation source. The laser intensity was modulated in the frequency range of 100 Hz to 2 MHz using an acousto-optic modulator (Crystal Technology 3080-120), driven by a waveform generator (Agilent 33522A). The laser beam diameter ($1/e^2$) was adjusted from approximately 2.8 mm at low modulation frequencies (100–1000 Hz) to about 1.8 mm at higher frequencies to optimize the signal producing periodic thermal excitation of the sample. Infrared thermal emission from the sample was collected and collimated using two gold-coated off-axis parabolic mirrors and focused onto a liquid nitrogen cooled mercury cadmium telluride (MCT) detector (Kolmar Technologies KMPV 11-1-J1/DC/Ge), sensitive in the 2-12 μm spectral range. The detector output was analyzed using a lock-in amplifier (Stanford Research Systems SR865), providing amplitude and phase information. Data acquisition and control were performed via computer. Before measurements, the system response and one-dimensional heat flow conditions were verified using reference glass and glassy carbon samples. Under conditions where the laser beam radius significantly exceeded the thermal diffusion length. The PTR signal corresponded to one-dimensional cross-plane thermal transport [19].

 doi:10.20944/preprints202603.1194.v1

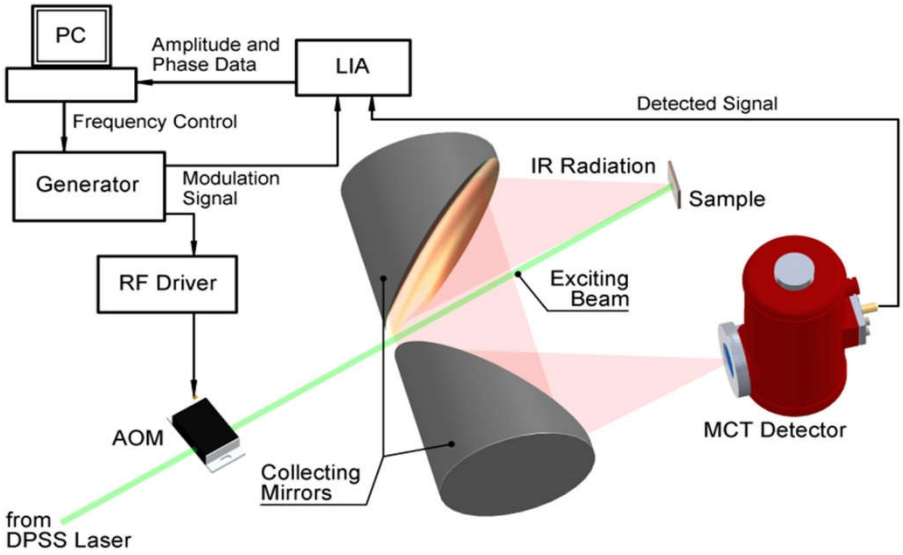

Figure 1. PTR experimental set-up used in the study [18].

In PTR detection, the laser spot is large compared to the sample thickness, so heat transport is essentially one-dimensional (along the z-axis). The one-dimensional heat-diffusion equation for harmonic excitation is [20]:

$$\frac{\partial T(z,t)}{\partial t} = \alpha \frac{\partial^2 T(z,t)}{\partial z^2}, \quad (1)$$

where $\alpha = k_\perp/\rho C$ is the thermal diffusivity. ρC is volumetric heat capacity of layers. The harmonic solution has the form $T(z,t) = Ae^{-\mu z} + Be^{\mu z}$, with $\mu = \sqrt{i\omega/\alpha}$

Each layer *n* is represented by a transfer matrix:

$$M_n = \begin{bmatrix} \cosh(\mu_n d_n) & \frac{\sinh(\mu_n d_n)}{k_{\perp,n}\mu_n} \\ -k_{\perp,n}\mu_n \sinh(\mu_n d_n) & \cosh(\mu_n d_n) \end{bmatrix}. \quad (2)$$

Where d_n is the layer thickness, $k_{\perp,n}$ is the cross-plane thermal conductivity.

For PTR, the detected signal is proportional to the surface temperature obtained from the 1D model:

$$\theta_{PTR} = -\frac{D}{C}. \quad (3)$$

C and *D* is defined as follows

$$\begin{bmatrix} A & B \\ C & D \end{bmatrix} = M_3 M_{32} M_2 M_{21} M_1$$

Experimental Results

A Hitachi SU-70 scanning electron microscope (SEM) was used to study the morphology of samples. The thickness of the layers was determined from cross-section SEM measurements (Figures 2 (a-d)). The layers obtained are continuous, and the interfaces between the ZnO:Cd,Eu layer and the sapphire substrate are well defined. The low amount of cadmium and europium doping was achieved during the growth process. In-depth Eu concentration profiles were measured on selected samples by Secondary Ion Mass Spectrometry (shown in figure 2(a1-d1)) but the Cd concentration was below detection limit (~10^{18} cm^{-3}) and Eu close to detection limits for this equipment and method. The measurements were performed with a CAMECA IMS6F system. Cd- and Eu-implanted ZnO layers were used as standards.

 doi:10.20944/preprints202603.1194.v1

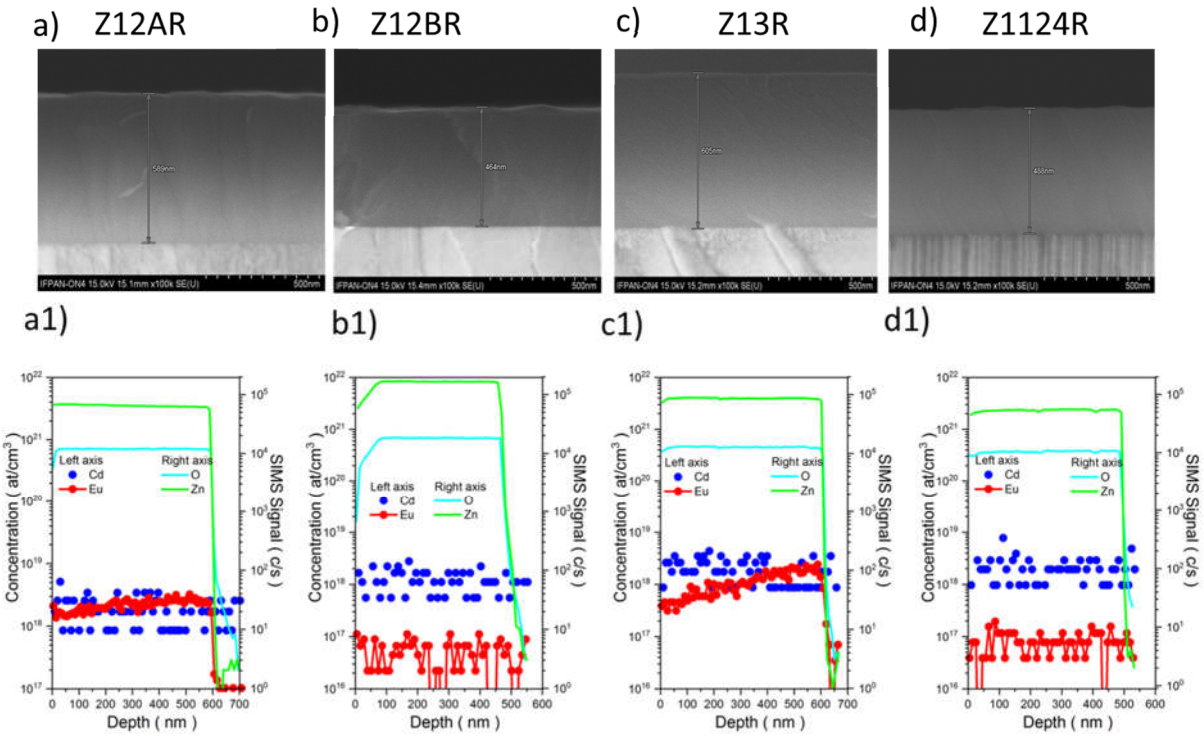

Figure 2. Cross-sectional SEM images (a-d) and corresponding SIMS depth profiles (a1-d1) for ZnO:Cd,Eu films: (a, a1) z12AR, (b, b1) z121BR, (c, c1) z13R, and (d, d1) z1124R. The SEM images indicate the film thickness, while the SIMS profiles show Cd and Eu concentrations (left axis) and Zn/O matrix signals (right axis) as a function of film depth.

The X-ray diffraction measurements were performed using a Panalytical X'Pert Pro MRD diffractometer equipped with a hybrid two-bounce Ge (2 2 0) monochromator and triple axis Ge (2 2 0) analyser in front of the detector. This equipment is equipped with a Cu-anode X-ray lamp that produces Cu $K_{\alpha 1}$ radiation (λ=1.54056 Å). The crystalline structural quality of the ZnO:Eu,Cd films deposited on r-Al_2O_3 was assessed by XRD. Figure 3 (a) presents the θ-2θ scans of all samples. The main peaks observed in the diffractograms are from reflections of 11.0 and 22.0 hexagonal ZnO atomic planes (JCPDS card no. 00-036-1451) and 01.2, 02.4, 30.6, 04.8 Al_2O_3 (substrate) atomic places (JCPDS card no. 00-042-1468) (Figure 3 a). Figures 3(b) and 3(c) present enlarged views of the ZnO (110) and (220) regions, respectively, highlighting systematic peak shifts relative to the reference ZnO peak positions. The MBE ZnO:Eu,Cd layers grow in *a*-direction as is expected on *r*-plane sapphire [21]. No other crystalline phases are detected indicating relatively high quality of the layers. The shift of diffraction peaks 11.0 and 22.0 indicates a change in the lattice constant "a". This type of behavior can be related to the addition of both Cd and Eu to the ZnO lattice [21].

Table 2. Lattice parameters "a" measured by X-ray diffraction.

Sample name	a (Å)
z12AR	3.2478
z12BR	3.2590
z13R	3.2527

 doi:10.20944/preprints202603.1194.v1

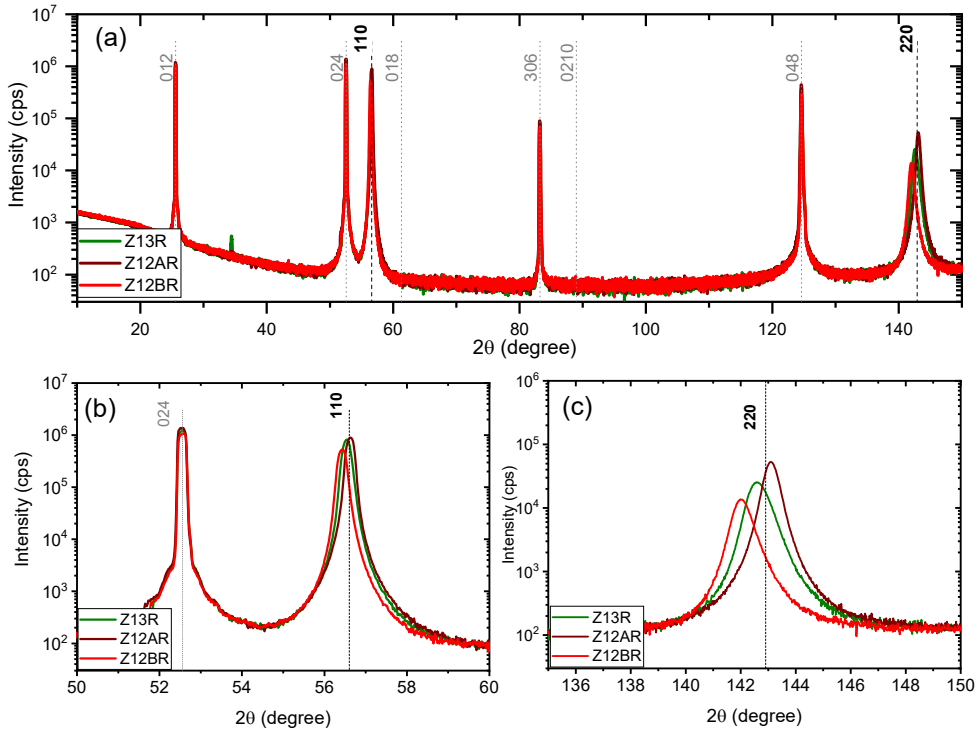

Figure 3. θ-2θ XRD patterns of the ZnO:Eu,Cd layers grown on r-Al_2O_3 (a) full scan; (b) and (c) enlarging the 110 and 220 peak areas to show their shift. The gray vertical doted lines indicate the position of Al_2O_3 peaks based on the JCPDS card no. 00-042-1468, whereas black doted lines indicate the position of ZnO peaks based on the JCPDS card no. 00-042-1468 .

The oxide films were analyzed with a UV–visible–infrared spectrophotometer to study their energy band gaps. Figure 4(a) shows transmittance spectra measured at room temperature. The cutoff for transmission is shifted. From the obtained transmission data, the absorption coefficient (α) was calculated using the equation, α = -d·ln T, where T is the transmittance and d is the samples thickness [22]. The ratio between the photon energy and the band gap (E_g) width is determined by the expression $(\alpha \cdot h\nu)^{1/n} = A(h\nu - Eg)$, where h is Planck's constant, ν is the photon's frequency and A is a proportionality constant. The allowed transitions dominate the basic absorption processes, giving n = 1/2 for direct transitions, typical of ZnO. The optical band gap can be obtained by extrapolation using a plot of $(\alpha \cdot h\nu)^2$ versus photon energy as shown in figure 4(b). It is widely known that doping Cd into ZnO material causes its energy gap to shift towards lower energy values [23]. The decrease in the band gap of Eu doped samples compared to pure ZnO can be due to a change in the electronic structure of ZnO due to the dilution of europium in its lattice. However, the blue shift of the band gap with an increase of Eu^{3+} concentration for ZnO:Eu films was observed by A. Singh et al [24].

 doi:10.20944/preprints202603.1194.v1

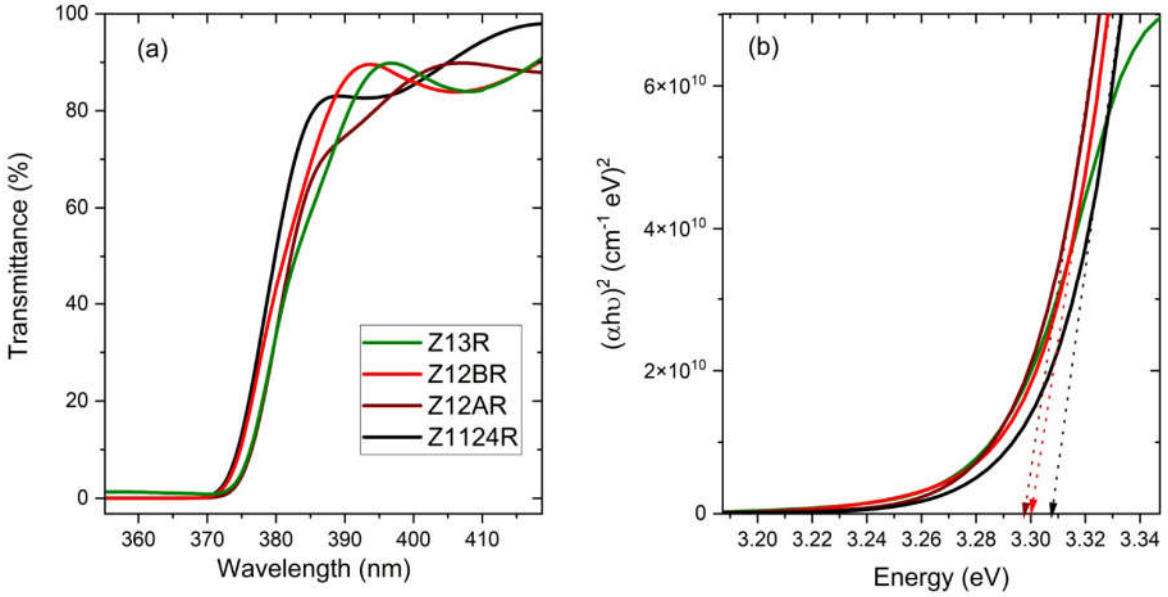

Figure 4. (a) Room temperature transmittance spectra of ZnO:Cd,Eu films. **(b)** $(\alpha \cdot h\nu)^2$ versus photon energy plot used to extract the direct optical band gap E_g.

Figure 5 shows the normalized room-temperature cathodoluminescence (CL) spectra of as-grown Eu-doped layers deposited on r-oriented sapphire. Samples exhibit ultra-violet emission at ~ 375±4 nm, which corresponds to near band edge radiative recombination [25] and a small emission at ~600 nm which is ascribed to Eu doping [26,27]. Usually, prior to annealing of the ZnO:Cd,Eu samples, no Es related emission is observed in this region.

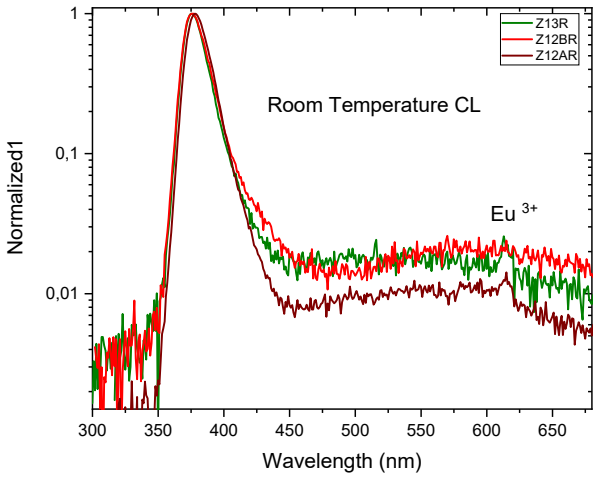

Figure 5. Normalized room-temperature cathodoluminescence (CL) spectra of *as-grown* samples.

PTR Results

Figures 6(a) and 6(b) show the normalized amplitude and normalized phase versus modulation frequency for four ZnCdO:Eu films (z1124R, z12AR, z121BR, and z13R). Experimental data are plotted as symbols, and the corresponding best-fit responses from fitting the complex PTR signal are shown as solid lines. The close overlap across the full frequency range indicates that the model accurately captures the sample thermal response, supporting the reliability of the extracted thermal

 doi:10.20944/preprints202603.1194.v1

parameters. From these fits, the thermal conductivity (k), thermal diffusivity (α), and thermal boundary resistance (R) are derived for the ZnO:Cd,Eu films, presented in table 3.

(a)

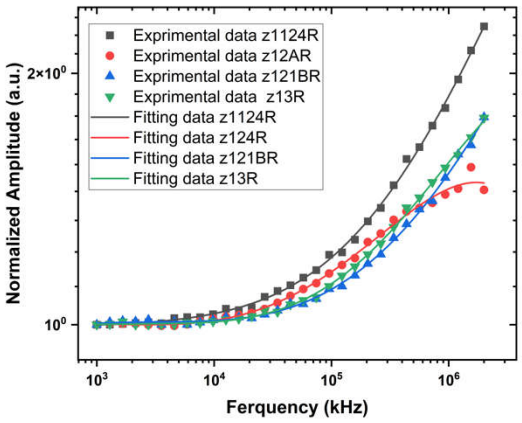

(b)

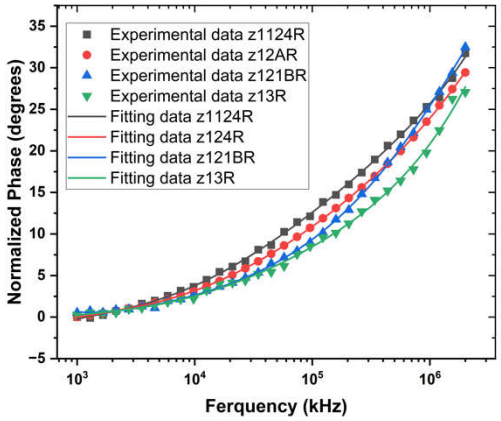

Figure 6. (a) Frequency-dependent normalized amplitude and (b) normaliezed phase with model fit of ZnO:Cd,Eu films.

Table 3. Summary of thermal conductivity (k), thermal diffusivity (α), and thermal boundary resistance (R) for ZnO:Cd,Eu films.

Sample name	Dopant concentration Cd,Eu ($\times 10^{19}$ cm^{-3})	Thermal conductivity (k) (Wm^{-1}K^{-1})	Thermal diffusivity (α) ($\times 10^{-6}$ m^2/s)	Thermal boundary resistance (R) ($\times 10^{-7}$ m^{2}KW^{-1})
z12AR	1.5	5.4	7.2	1.9
z121BR	0.5	6.3	7.5	2.6
z13R	1.3	3.7	7.0	1.6
z1124R	0.3	6.2	7.0	2.2

Dopant-Dependent Thermal Conductivity

The thermal conductivity shows an overall decrease with increasing dopant concentration in ZnO:Cd,Eu. The lowest-doped films exhibits the largest k (~6.2–6.3 W·m^{-1}·K^{-1}), while higher dopant contents reduce k (to ~3.7 W·m^{-1}·K^{-1} at 1.5×10^{19} cm^{-3}) shown in Figure 7. This trend is consistent with enhanced phonon scattering caused by increased disorder and dopant-related defects in the ZnO lattice at higher concentrations. The error bars represent the uncertainty from the fitting

 doi:10.20944/preprints202603.1194.v1

procedure, indicating that the reduction in k at higher doping concentrations is larger than the estimated measurement uncertainty.

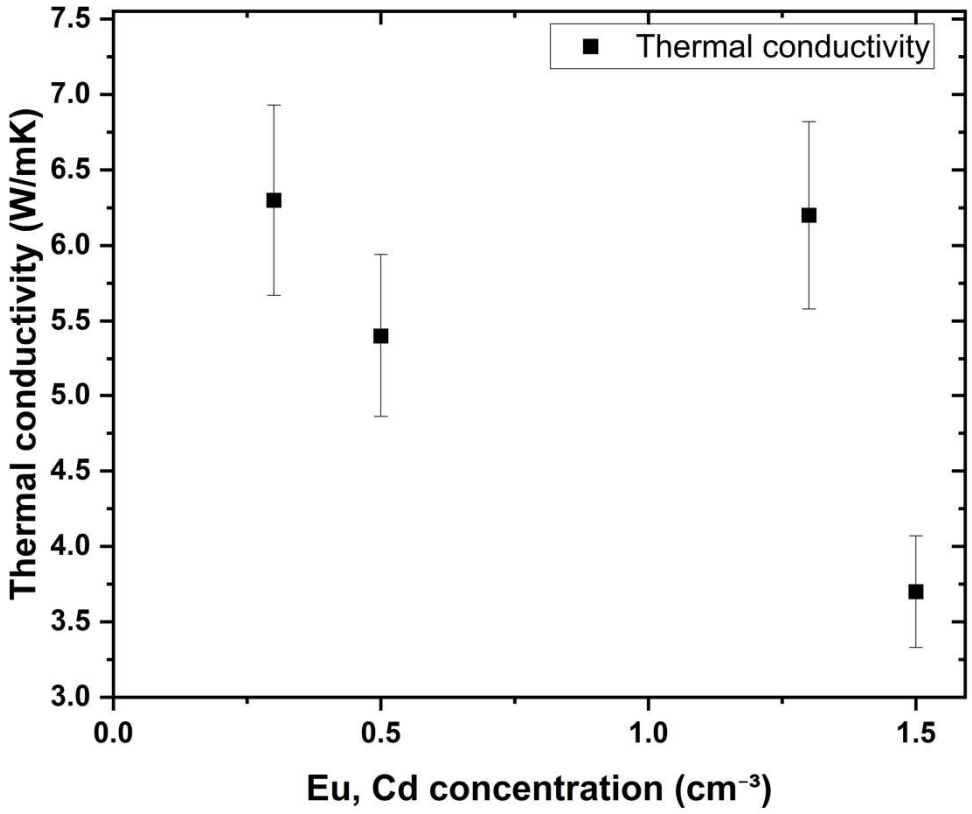

Figure 7. Thermal Conductivity of ZnO:Cd,Eu as a Function of Dopant Concentration.

Thermal conductivity does not scale monotonically with dopant content across the ZnCdO:Eu films, indicating that heat transport is governed by dopant incorporation uniformity and associated defect microstructure. Non-homogeneous incorporation of Cd and Eu (and the associated Zn/O matrix disorder) together with depth-dependent concentration gradients generates spatial fluctuations in strain and defect density, increasing phonon scattering. For cross-plane transport, such gradients create a series-resistance effect, so the measured thermal conductivity represents an effective value dominated by lower k regions. Consequently, samples with similar nominal Cd/Eu levels such as z12AR (1.5×10^{19} cm^{-3}) and z13R (1.3×10^{19} cm^{-3}) can exhibit markedly different thermal conductivity **(**~3.7 vs ~6.2 $W\cdot m^{-1}\cdot K^{-1}$**)**, while lower-content films like z1124R (3×10^{18} cm^{-3}) and z121BR (5×10^{18} cm^{-3}) show higher k **(**~6.3 and ~5.4 $W\cdot m^{-1}\cdot K^{-1}$**)**, depending on the degree of Cd/Eu uniformity, clustering, and the resulting phonon scattering in the ZnO lattice.

Conclusions

The MBE method was used to produce high-quality epitaxial layers of non-polar ZnO (*a*-oriented) doped *in situ* with trace amounts of Eu and Cd. Despite the Cd and Eu content in these samples being at the detection limit of the SIMS method, a change in the lattice constants and energy gap of these layers was registered. Furthermore, at room temperature, a weak luminescence characteristic of red emission originating from the presence of Eu 3+ ions is observed for non-annealed samples. Even small amounts of Eu and Cd impurities affect the thermoelectric properties of these layers, which is a motivation for further research in this area. From the thermal

 doi:10.20944/preprints202603.1194.v1

measurements, it is concluded that doping level has minimal influence on thermal conductivity values. However, the in-depth dopant profiles depend strongly on the thermal conductivity values.

Acknowledgments: This work was supported in part by the Polish National Science Center, Grants No. 2021/41/B/ST5/00216. C.J. Tavares acknowledges the funding from the Portuguese Foundation for Science and Technology (FCT) in the framework of the Strategic Funding UID/04650/2025, https://doi.org/10.54499/UID/04650/2025.

References

1. Cho, J. Antibacterial applications of TiO_2-based hybrid semiconductor nanomaterials: Recent advances and future prospects. In *Titanium dioxide-based multifunctional hybrid nanomaterials: Application on health, energy and environment*, 2nd ed.; Parakash, J.; Springer: cham, Switzerland, 2025, pp. 313-337.
2. Demissie, T. B.; Alebachew, N.; Murthy, H. C. A. Historical Background of Multifunctional Inorganic Materials and Their Applications. In *Multifunctional Inorganic Nanomaterials: Synthesis, Properties, and Applications*; Ananda Murthy, H. C., Subramaniam, V., Sillanpää, M. E. T., Balachandran, G., Hegde, G., Eds.; CRC Press: Boca Raton, FL, USA, 2025, pp.1-20.
3. Hussain, I.; Amna, R.; Kalidasan, B.; Rani, G. M.; Bandi, H.; Venkateswarlu, S.; Khan, S. A.; Mohapatra, D.; Zhang, K. MXenes for Various Applications: Recent Trends and Future Aspects. *SmartMat* **2025**, *6*, e70012.
4. Han, H.; Zhao, L.; Wu, X.; Zuo, B.; Bian, S.; Li, T.; Yu, L. Advancements in Thermoelectric Materials: Optimization Strategies for Enhancing Energy Conversion. *J. Mater. Chem. A* **2024**, *12*, 24041-24083.
5. Saeed, M.; Marwani, H. M.; Shahzad, U.; Asiri, A. M.; Rahman, M. M. Recent Advances, Challenges, and Future Perspectives of ZnO Nanostructure Materials towards Energy Applications. *Chem. Rec.* **2024**, *24*, e202300106.
6. Saleem, S.; Khalid, S.; Malik, M. A.; Nazir, A. Review and Outlook of Zinc Sulfide Nanostructures for Supercapacitors. *Energy Fuels* **2024**, *38*, 9153-9185.
7. Kumar, S.; Madhuri, R. Fundamentals for Material and Nanomaterial Synthesis. In *Green Sustainable Process for Chemical and Environmental Engineering and Science*; Elsevier: Amsterdam, The Netherlands, 2021; pp.137-169.
8. Nallasani, U. R.; Diep, N. Q.; Lin, C.-Y.; Huynh, T. B. T.; Tran, Q. T.; Wang, H.-J.; Zhou, X.; Saurabh, S. Monolithic Integration of 2D GaSe/3D β-Ga_2O_3 Mixed-Dimensional Heterostructures on c-Sapphire Substrates by Molecular Beam Epitaxy. *ACS Appl. Electron. Mater.* **2025**, *7*, 7827-7837.
9. Rahman, M. H.; Rahaman, M. Z.; Chowdhury, E. H.; Motalab, M.; Hossain, A. K. M. A.; Roknuzzaman, M. Understanding the Role of Rare-Earth Metal Doping on the Electronic Structure and Optical Characteristics of ZnO. *Mol. Syst. Des. Eng.* **2022**, *7*, 1516-1528.
10. Korotcenkov, G. Cd- and Zn-Based Wide Band Gap II–VI Semiconductors. In *Handbook of II–VI Semiconductor-Based Sensors and Radiation Detectors: Volume 1, Materials and Technology*; Springer: Cham, Switzerland, 2023; pp. 21-65.
11. Qiu, G.; Li, T.; Xu, X.; Liu, Y.; Niyogi, M.; Cariaga, K.; Oses, C. High Entropy Powering Green Energy: Hydrogen, Batteries, Electronics, and Catalysis. *npj Comput. Mater.* **2025**, *11*, 145.
12. Kumar, M.; Singh, G.; Chauhan, M. S. Europium (Eu^{3+})-Doped ZnO Nanostructures: Synthesis, Characterization, and Photocatalytic, Chemical Sensing and Preliminary Assessment of Magnetic Properties. *Ceram. Int.* **2021**, *47*, 17023-17033.
13. Zheng, B.; Fan, J.; Chen, B.; Qin, X.; Wang, J.; Wang, F.; Deng, R.; Liu, X. Rare-Earth Doping in Nanostructured Inorganic Materials. *Chem. Rev.* **2022**, *122*, 5519–5603.
14. Wang, H.; Chen, L.; Wu, Y.; Li, S.; Zhu, G.; Liao, W.; Dong, W. Advancing Inorganic Electro-Optical Materials for 5G Communications: From Fundamental Mechanisms to Future Perspectives. *Light Sci. Appl.* **2025**, *14*, 190.
15. Lyu, W.-Y.; Liu, W.-D.; Li, M.; Hong, M.; Guo, K.; Luo, J.; Xing, J.; Sun, Q.; Xu, S.; Zou, J.; Chen, Z.-G. The Effect of Rare Earth Element Doping on Thermoelectric Properties of GeTe. *Chem. Eng. J.* **2022**, *446*, 137278.

 doi:10.20944/preprints202603.1194.v1

16. Yang, S.; She, X.; Wang, Z.; Xiong, T.; Zheng, Z.; Feng, B. The Influence Mechanism of High-Valence Rare Earth Element Doping on the Thermoelectric Properties of ZnO. *J. Mater. Sci.: Mater. Electron.* **2024**, *35*, 1139.
17. Correia, F. C.; Ribeiro, J. M.; Ferreira, A.; Reparaz, J. S.; Goñi, A. R.; Boll, T.; Mendes, A.; Tavares, C. J. The Effect of Bi Doping on the Thermal Conductivity of ZnO and ZnO:Al Thin Films. *Vacuum* **2023**, *207*, 111572.
18. Cabrera, H.; Zumeta-Dubé, I.; Korte, D.; Grima-Gallardo, P.; Alvarado, F.; Aitken, J. A.; A Brant, J. A.; Zhang, J. H.; Calderon, A.; Marin, E.; Aguilar-Frutis, M.; Erazo, J. E.; Perez-Cappe, E.; Franko, M. Thermoelectric Transport Properties of $CuFeInTe_3$. J Alloy Compd. **2015**, 651, 490.
19. Chatterjee, A.; Swapna, M.S.; Mikaeeli, A.; Khalid, M.; Korte, D.; Wieck, A.D.; Pawlak, M. Photothermal Infrared Radiometry and Thermoreflectance-Unique Strategy for Thermal Transport Characterization of Nanolayers. *Nanomaterials* 2024, *14*, 1711.
20. Pawlak, M.; Jukam, N.; Kruck, T.; Dziczek, D.; Ludwig, A.; Wieck, A. D. Measurement of Thermal Transport Properties of Selected Superlattice and Thin Films Using Frequency-Domain Photothermal Infrared Radiometry. *Measurement* **2020**, *166*, 108226.
21. Venkatachalapathy, V., Galeckas, A., Trunk, M., Zhang, T., Azarov, A., & Kuznetsov, A. Y. (2011). Understanding phase separation in ZnCdO by a combination of structural and optical analysis. Physical Review B—Condensed Matter and Materials Physics, 83(12), 125315.
22. Lysak, A.; Przeździecka, E.; Wierzbicka, A.; Jakiela, R.; Khosravizadeh, Z.; Szot, M.; Adhikari, A.; Kozanecki, A. Temperature Dependence of the Bandgap of Eu Doped $\{ZnCdO/ZnO\}_{30}$ Multilayer Structures. *Thin Solid Films* **2023**, *781*, 139982.
23. Jiang, J.; Zhu, L.; Li, Y.; Guo, Y.; Zhou, W.; Cao, L.; He, H.; Ye, Z. Band Gap Modulation of ZnCdO Alloy Thin Films with Different Cd Contents Grown by Pulsed Laser Deposition. *J. Alloys Compd.* **2013**, *547*, 59-62.
24. Singh, A.; Arya, P.; Choudhary, D.; Kumar, S.; Srivastava, A. K.; Singh, I. B. Cost-Effective ZnO-Eu^{3+} Films with Efficient Energy Transfer between Host and Dopant. *SN Appl. Sci.* **2020**, *2*, 870.
25. Przeździecka, E.; Paradowska, K. M.; Lysak, A.; Wierzbicka, A.; Sybilski, P.; Płaczek-Popko, E.; Jakiela, R.; Sajkowski, J.; Kozanecki, A. Influence of As Doping on the Properties of Nonpolar ZnO. *Thin Solid Films* **2021**, *720*, 138520.
26. Lysak, A.; Przeździecka, E.; Wierzbicka, A.; Jakiela, R.; Khosravizadeh, Z.; Szot, M.; Adhikari, A.; Kozanecki, A. Temperature Dependence of the Bandgap of Eu Doped $\{ZnCdO/ZnO\}_{30}$ Multilayer Structures. *Thin Solid Films* 2023, *781*, 139982.
27. Mathew, J.A.; Tsiumra, V.; Sajkowski, J.M.; Wierzbicka, A.; Jakiela, R.; Zhydachevskyy, Y.; Przeździecka, E.; Stachowicz, M.; Kozanecki, A. Photoluminescence of Europium in ZnO and ZnMgO Thin Films Grown by Molecular Beam Epitaxy. *J. Lumin.* 2022, *251*, 119167.